Journal of Power Sources 629 (2025) 236044

Contents lists available at ScienceDirect

Journal of Power Sources

journal homepage: www.elsevier.com/locate/jpowsour

Thermo-electrochemical characterization of a commercial $LiNi_{0.8}Co_{0.15}Al_{0.05}O_2$ /Graphite+Si 18650 cell

Patrick J. West [a,b], Nicolas Leport [c], Dillon Hayman [d], Rachel Carter [a], Corey T. Love [a], Laurent Pilon [c,e,f], Gordon H. Waller [a,*]

[a] Chemistry Division, U.S. Naval Research Laboratory, Washington, D.C, USA
[b] American Society of Engineering Education, Washington, D.C, USA
[c] Mechanical and Aerospace Engineering Department, Henry Samueli School of Engineering and Applied Science, University of California, Los Angeles, CA, 90095, USA
[d] Excet Inc. Springfield, VA, USA
[e] California NanoSystems Institute, University of California, Los Angeles, CA, 90095, USA
[f] Institute of the Environment and Sustainability, University of California, Los Angeles, CA, 90095, USA

HIGHLIGHTS

- Coupled thermo-electrochemical characterization of a commercial 18650 cell.
- Demonstrated form-factor agnostic measurements of entropic potentials.
- Observed transition between reversible heat and joule heat dominated regimes.
- Correlated full cell endothermic heat flow with anode-side electrochemistry.

GRAPHICAL ABSTRACT

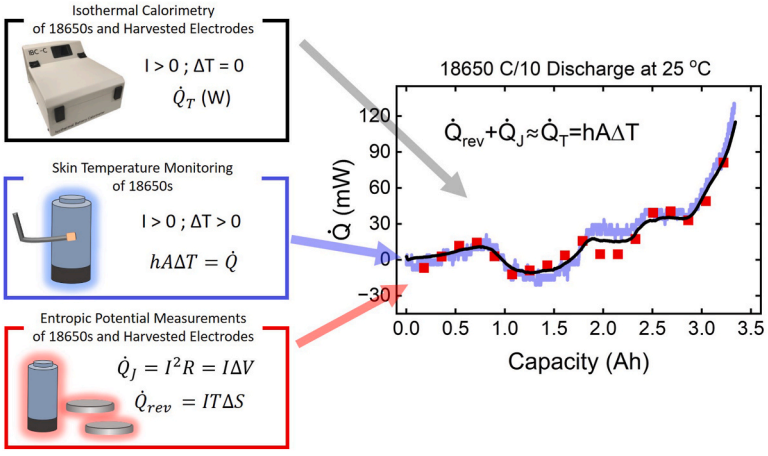

ABSTRACT

Understanding the interplay between battery operation and heat generation is key to the thermal management and safe deployment of Li-ion batteries. Herein, we combine isothermal calorimetry, cell surface temperature monitoring, and electrochemically derived thermodynamic metrics to present the thermo-electrochemical characterization of a commercial $LiNi_{0.8}Co_{0.15}Al_{0.05}O_2$/Graphite + Si 18650 cell. This combined thermo-electrochemical approach enabled the tracking of heat generation sources as a function of C-rate (C/20-1C) to determine the boundary between reversible heat, $\dot{Q}_{rev}$, dominated and joule heating, $\dot{Q}_J$, dominated operation conditions. By comparing heat generation during continuous and intermittent operation, activation energies were calculated. Entropic potential measurements of the 18650 and of harvested elec-

* Corresponding author.
E-mail address: gordon.h.waller.civ@us.navy.mil (G.H. Waller).

https://doi.org/10.1016/j.jpowsour.2024.236044
Received 12 August 2024; Received in revised form 18 November 2024; Accepted 6 December 2024
Available online 12 December 2024
0378-7753/Published by Elsevier B.V.

trodes half-cells enabled identification of electrode specific heat generation features, like the discharge endotherm, to be attributed to electrode-specific processes. Additionally, isothermal heat generation and surface temperature measurements were reconstituted via a modified Newton's law of cooling. This work cumulated in the reconstruction of the isothermal heat generation profile from $\dot{Q}_{rev}$ and $\dot{Q}_J$ during C/10 cycling at 25 °C, bridging the divide between thermodynamic and experimental heat generation values.

1. Introduction

Portable electrochemical energy storage systems, like Li-ion batteries (LIBs), have enabled the implementation of a wide array of electronics through their diversity of sizes and form factors, spanning from academic coin (<60 mAh) to commercial cylindrical 18650 cells (1–4 Ah) and beyond [1,2]. As cells increase in size, management strategies are critical for balancing electrochemical performance with thermal phenomena like operational heat generation, cell temperature rises, and thermal safety [3,4]. At the lab scale, coin cell experimentation can benchmark electrochemical performance, however calorimetric investigations of coin cells often only output heat generation on the order of mW due to low active mass to casing ratio of coin cells [5]. While at the industrial scale, thermocouple data of large arrays of 18650's can provide real time thermal data during real-world operation in fluctuating thermal environments.

Linking lab scale testing and commercial testing is further complicated through variations in cell testing conditions, such as operating temperature and environmental cooling conditions, as well as differences in cell configuration. While the cylindrical 18650 cell jelly roll design achieves high mass loadings that enables them to meet industry performance metrics, mainly delivered capacity and capacity retention, it is distinct from the single layer electrodes used in academic coin cells, and the larger electrode size and metal can complicates many of the more facile operando characterization techniques which focus on small volumes of the active material. Furthermore, to preserve industrial intellectual property, details like the electrode formulation mass loadings, and electrolyte formulation and electrolytes used in 18650s are not disclosed by manufacturers. Moreover, even when harvested electrodes from 18650s are tested in coin cells or pouch cells, it is difficult to recreate the same electrochemical environment as in an 18650 due to variations in stack pressure, free electrolyte, and unintentional chemical changes to the electrode during harvesting. Still, thermodynamic properties should be intrinsic materials properties if tested for in highly controlled conditions like isothermal calorimetry and thus form-factor agnostic. In fact, commercially produced 18650s are good candidates for isothermal battery calorimetry (IBC) testing as they provide more electrochemically active mass per total thermal mass enabling the probing of heat generation at across multiple C-rates.

Heat generated during electrochemical operation can be exothermic or endothermic as the cell generates or absorbs heat [6]. During IBC testing, isothermal conditions are maintained by a Peltier heating element which adds or removes heat to the chamber at an equal rate to the total heat generation of the cell, $\dot{Q}_T$ in Watts. Heat generated by an electrochemical cell during operation is the summation of multiple heat sources [7]:

$$\dot{Q}_T = \dot{Q}_{rev} + \dot{Q}_J + \dot{Q}_{mix} + \dot{Q}_{sr} \tag{1}$$

where $\dot{Q}_{rev}$ is the reversible heat generation, $\dot{Q}_J$ is joule heating, $\dot{Q}_{mix}$ is the heat of mixing, and $\dot{Q}_{sr}$ is the heat of side reactions of the electrochemical system. $\dot{Q}_{rev}$ is the heat associated with the target electrochemical reaction and can be described as:

$$\dot{Q}_{rev} = IT\Delta S = IT\frac{\partial U_{OCV}(x)}{\partial T} \tag{2}$$

where I is the applied current, T is the operating temperature, ΔS is the entropic potential, and $U_{OCV}(x)$ is the open circuit voltage of the cell at Li content (x). The relationship between an electrochemical reaction's thermodynamics and voltage are outlined via Gibbs free energy (ΔG):

$$G_{Li}^{cathode} - G_{Li}^{anode} = \Delta G = -nFE = -nFU_{OCV}, \tag{3}$$

and

$$G = -SdT + Vdp + \sum \mu_i dn_i, \tag{4}$$

Where, n is the number of electrons, F is Faraday's constant, S is entropy, T is temperature, V is volume, p is pressure, μ_i is chemical potential, and n is the chemical composition. Taking the partial derivative of equation (3), with respect to temperature at a constant pressure and chemical compositions yields ΔS in mV/K [7,8]:

$$\Delta S = \left(\frac{\partial \Delta G}{\partial T}\right)_{p,n} = \frac{\partial U_{OCV}}{\partial T}. \tag{5}$$

$\dot{Q}_{rev}$ is dependent on the directionality of the current (positive or negative) and therefore can be endothermic or exothermic [9]. If the system were fully thermally reversible and had no path dependence, then $\dot{Q}_{rev}$ would account for all heat on charge and discharge such that $\dot{Q}_T = \dot{Q}_{rev}$, and heat generation would be equal in magnitude and opposite in direction for charge and discharge. In other words, the net heat generation would be zero. In reality, electrochemical resistances and overpotentials also generate heat, as described by $\dot{Q}_J$:

$$\dot{Q}_J = I(V_{redox} - U_{OCV}) = I\eta = I^2R(x) \tag{6}$$

where V_{redox} is the redox potential, η is the overpotential, and R(x) is the resistance of the system with respect to Li content (x). Unlike $\dot{Q}_{rev}$, $\dot{Q}_J$ is always exothermic regardless of the directionality of the applied current. $\dot{Q}_J$ and R(x) can be found experimentally through the comparison of rest and active potentials, or through the computation of resistance values as a function of SoC [10,11].

The heat of mixing, $\dot{Q}_{mix}$, describes the energy required to mix two or more constituents into a homogenous blend and originates from ion concentration gradients. These gradients can be (i) in the electrolyte [12,13], (ii) in the electrode due to non-uniform current distribution [14], (iii) within vacancies in the electrode [15], and/or (iv) within intercalated Li in the electrode due to electrochemical reactions [16]. Generally, the heat of mixing is dominated by the ionic concentration gradient of intercalated Li:

$$\dot{Q}_{mix}(x,T) = -\int_{V_\infty}\sum_i \left[\overline{h_i}(x,T) - \overline{h_i^{avg}}(x,T)\right]\frac{\partial c_i}{\partial t}\mathrm{d}V. \tag{7}$$

where V_∞ is the volume of the cell, $\overline{h_i}$ (x, T) is the partial molar enthalpy of species i and the superscript "avg" refers to the partial molar enthalpy corresponding to the volume-averaged concentration, and c_i is the local concentration of species i. In electrochemical systems, high C-rates can induce large concentration gradients of Li-ions at an active materials' particle surface [17]. The built-up Li-ions generate heat as they perform work to uniformly disperse through the crystal structure. $\dot{Q}_{mix}$ can account for as much as 20 % of $\dot{Q}_T$ during 6C charging of transition metal oxide cathodes [18], but is often considered negligible at lower rates.

The heat generation associated with unwanted side reactions, $\dot{Q}_{sr}$, is most prevalent during the formation of electrode/electrolyte interfaces during the initial cycles after cell fabrication [19]. Once a stable

interface has formed, careful control of the cell's operation voltage window and C-rate can ensure minimal additional side reactions, also minimizing $\dot{Q}_{sr}$.

Cells are rarely operated in isothermal conditions and thus their operational heat generation can result in self-heating. In many cases, cells have some sort of active thermal management to mitigate temperature rise. Self-heating under convective cooling can be rationalized through a slight modification of Newton's law of cooling:

$$\Delta T = \dot{Q}_T/(hA), \tag{8}$$

where ΔT is the difference between the cell's surface temperature and the bulk fluid temperature, h is the convective heat transfer coefficient (W/m^2K) and A is the surface area of the cell (m^2). In other words, self-heating is the result of the internal heat generation rate, $\dot{Q}_T$, outpacing the rate of cooling provided by the operational conditions. Heat transfer coefficients are approximated to be between 2 and 25 W/m^2K for the free convection of gases and between 25 and 250 W/m^2K for the forced convection of gases [20]. Similar methodologies have been presented before, like the cell cooling coefficient by Hales et al. [21]

Intercalation-based Li-ion batteries rely on the reversible shuttling of Li^+ ions between an anode and cathode to provide electrochemical energy. In an ideal scenario, the cell's measured voltage would be dictated only by the theoretical potential of the redox reaction, E^0, occurring [22]. In practice, there are multiple undesired processes that influence the observed voltage [23]:

$$E_{observed} = E^0_{rxn} + \eta_{ohmic} + \eta_{act} + \eta_{con} + \eta_{sr} \tag{9}$$

ohmic polarization, $\eta_{ohmic} = (V_{ohmic} - U_{OCV})$, estimates the electronic resistance of the system through the difference between the U_{OCV} and the potential immediately following the application of a current, V_{ohmic}. Activation overpotential, η_{act}, encompasses the additional energy required to overcome the activation energy barrier as described through the Butler-Volmer reaction and Tafel Kinetics. Concentration overpotential, η_{con}, relates mass transport limitations from the electrolyte to the electrode surface through the Nernst-Plank Equations and the Cottrell Equation.

All three of these overpotentials are directly proportional to the applied current: as the current decreases so too do η_{ohmic}, η_{act}, and η_{con} [23]. By comparing Equations (1), (2), (6) and (9), a link can be drawn between electrochemistry and heat generation that serves as the basis for much of the theoretical calculations of LIB heat generation analyses [5]. Electrochemically derived heat calculations rely on comparison between rest and operational voltages, therefore only giving information at discrete SoCs. By contrast, IBC and skin temperature measurements provide operando information. When used in tandem, these three approaches can provide wholistic thermal information of the target electrochemical system: $LiNi_{0.8}Co_{0.15}Al_{0.05}O_2$ (NCA)/Graphite + Si.

The NCA/Graphite + Si system is a mature LIB chemistry currently deployed in many commercial applications, like electric vehicles and personal electronics. Along with $LiCoO_2$, $LiNiO_2$, and $LiNi_xMn_yCo_zO_2$, NCA is a transition metal oxide cathode material composed of layers of edge and corner sharing MO_6 octahedra layers with stabilizing Li ions in its interlayer region [24]. The two degrees of freedom of the interlayer region allow for repeated (de)insertion of Li ions to transition metal redox sites during electrochemical operation. However, excessive removal of Li-ion from the layered structure is accompanied by energetically unfavorable and often irreversible crystallographic transitions [25–27]. In the NCA system, reversible delithiation up to $Li_{0.2}$NCA is commonly reported [28–30], while accessing lower Li contents is possible through controlled chemical doping [31]. As shown by Nam et al., NCA capacity retention is also highly dependent on transition metal stoichiometry, with a $LiNi_{0.8}Co_{0.156}Al_{0.04}O_2$ cathode providing higher capacity retention, albeit at the cost of a lower initial capacity, than higher Ni content competitors [32]. In the commercial space, Ni contents hover around 0.8 to balance delivered capacities and retention metrics [33–35].

On the anode side, graphite remains one of the most widely-used commercial anode materials for LIBs. Like its cathode counterpart, graphite can reversibly accommodate Li ions into its interlayer resulting in many intermediate stages of lithiated graphite ranging from dilute (Li_xC_6; $x > 0.1$) to stage 4 ($Li_{0.1}C_6$), stage 3 ($Li_{0.2}C_6$), stage 2 ($Li_{0.5}C_6$), and stage 1 (LiC_6), for a high specific capacity of 372 mAh/g [36,37]. These first-order phase transitions manifest electrochemically as series of galvanostatic voltage plateaus that are more discrete on lithiation than delithiation [38]. The addition of Si, 4200 mAh/g [39], to form blended Graphite + Si anodes provides a route to further optimize anode energy density [40]. However, Si undergoes significant volume expansion and path dependent lithiation mechanisms resulting in a voltage hysteresis [41,42]. Still, the NCA/graphite + Si system has seen wide adoption in both commercial and academic settings [28,39,43,44].

There are multiple published thermodynamic and calorimetric studies of graphite [8,45], Si [46,47], NCA [48] and other LIB electrode materials [49]. Wojtala et al. [44] has shown the entropic potentials of a NCA/Graphite + Si 18650 as a function of SoC and aging. Moreover, they were able to decouple anode and cathode entropic contributions by repeating entropic measurements on harvested electrode coin cells. Calorimetric studies of Li-ion coin cells highlight how calorimetry can be used to identify path-dependent electrochemistry [50] and decouple $\dot{Q}_{rev}$ from $\dot{Q}_J$ during electrochemical redox [51]. Building off of this foundation, we present a non-destructive thermo-electrochemical interrogation of a NCA/Graphite 18650's across a wide range of applied currents: 1C to C/20. The rate dependencies of the system's voltage and heat generation behavior under continuous and intermittent operation were used to identify $\dot{Q}_{rev}$ dominated operating conditions. Then, entropic potential measurements of the 18650 full cell and harvested electrodes in half cell coin cells identified electrode specific heat generation phenomena. Ultimately, IBC testing served as the link to reconcile electrochemically-derived $\dot{Q}_{rev}$ and $\dot{Q}_J$ values with operational skin temperature rise of the 18650 to bridge theoretical and experimental discrepancies.

2. Materials and methods

2.1. Electrochemical testing of 18650 cells

Electrochemical testing was performed on a commercial 18650 cylindrical cell with an NCA based cathode and a mixed graphite + Si anode. C-rates were determined from the manufacturer specified capacity of 3.4 Ah. During rate capability testing, cells were cycled between 2.5 and 4.2V under constant current constant voltage (CC-CV) charging conditions, wherein cells were galvanostatically charged to 4.2V at the target C-rate, then held at 4.2V until a C/20 current (0.17 mA) was observed. Testing was performed either in an isothermal battery calorimeter (IBC-C, Thermal Hazard Technology) or in a temperature-controlled battery testing chamber (MACCOR). The IBC was set to maintain an isothermal condition of 25 °C by means of a Peltier-cooler attached to an aluminum heat sink with a semi-cylindrical recess. Individual 18650 cells are mounted into the IBC heat sink using thermally conductive paste. The battery testing chamber temperature was set to 25 °C, the fan-powered cooling system was activated whenever a thermocouple at the top of the chamber deviated from the set temperature. Thermal couples were taped to the side of each cell to track skin temperature during cycling. Chamber positions were noted for each cell.

Hybrid Pulse Power Characterization (HPPC) measured resistance in a variety of testing procedures such as those described in the NRL [52], USABC [53], and INL [54] battery test manuals. HPPC measures the cell voltage while delivering a brief high-amplitude, current pulse. The cell is assumed to be near equilibrium just before the pulse with an ohmic relationship between current and voltage over the pulse period. The cell

resistance is calculated using the current pulse amplitude (I) as well as the starting voltage (V_1) and ending voltage (V_2). The cell resistance can be calculated as:

$$R_{DC} = \frac{V_1\text{-}V_2}{I} \tag{10}$$

During HPPC testing, fully charged cells were placed in a battery testing chamber at 25 °C and rested for 1 h to reach thermal and electrochemical equilibrium. Each HPPC step was composed of an initial 30-s 1C CC discharge pulse, a 40-s rest, and a 10-s 0.75C CC charging pulse. Cell were then discharged for 10 % of their rated capacity (0.34 Ah) at C/3. The HPPC step protocol was repeated until the cell discharged to 10 % SoC.

Galvanostatic intermittent titration technique (GITT) testing of the 18650s, was performed two ways. First, for IBC-coupled testing at 25 °C, cells were (dis)charged for 30 min at a C/10 rate, corresponding to a 5 % change in SoC, followed by a 4-h rest, before continual cycling until either voltage limit, 4.2V or 2.5V, was reached. The second GITT method was performed to measure entropic potentials. 18650 cells were (dis) charged for 30 min at a C/10 rate, corresponding to a 5 % change in SoC, followed by a 24-h rest at 25 °C. Then, the cell was held at 15, 20, 25, 30, and 35 °C for 4 h each, before returning to 25 °C for 4 h for further cycling. Differential voltage (dV/dt) analysis was performed on the temperature modulation steps to ensure that an electrochemical equilibrium was achieved after each change in temperature, **Fig. S1**.

2.2. Materials characterization

Electrodes were harvested from fresh 18650 cells after three C/20 cycles between 2.5 and 4.2V, ending in the discharged state. Disassembly was performed under argon gas by cutting cells open at the spin groove with a pipe-cutter. After drying under vacuum for 24 h, the cell casing was cut laterally, and the jelly roll was removed. Following separation of the two electrodes, electrodes were cut into 8 cm strips and rinsed using dimethyl carbonate (DMC). One side of the electrode coating was removed using a methanol-soaked lint-free cloth and electrodes were punched to size for use in coin cells. The total area including both sides of the 18650 electrodes was 760 cm^2 and 809 cm^2 for the cathode and anode, respectively. The chemical composition of harvested electrodes was confirmed via energy dispersive spectroscopy (EDS), Table S1 and Table S2. The cathode had a cation ratio of 0.79/0.14/0.06 Ni/Co/Al, while the anode had an 95/5 ratio of C/Si. No evidence of Mn was found via EDS.

Harvested cathodes were assembled into Li-metal half-cell coin cells using 1 M $LiPF_6$ in 50/50 vol% ethylene carbonate/diethyl carbonate that was deemed to be generic and analogous to most commercial electrolytes. After 3 cycles at C/10, between 3.0 and 4.2 V vs Li, the cells were discharged to various voltages along the discharge profile: 3.5, 3.8, 4.05, 4.2V vs Li, ***Fig. S2***. The harvested cathode coin cells delivered 4.42 mAh/cm^2 capacity, and were considered comparable to that of the 18650's delivered 3.4 Ah or 4.49 mAh/cm^2 of the cathode. The cathodes were recovered from the coin cells under argon, rinsed with DMC, and then dried under vacuum. The coin cell cycled electrodes were then sealed between Kapton tape before X-ray diffraction (XRD). XRD was performed between 5 and 90° 2θ using a Smartlab (Rigaku) X-ray diffractometer. XRD patterns were normalized to the constituent peak and index using the PDXL software. The Ex-situ XRD confirms the characteristic (003), (104), (108), and (110) peaks of layered NCA material, along with the expected trends. Notably, at higher voltage, the (003) shifts to lower 2θ, the (104) shifts to higher 2θ, and the (108)/(110) doublet broadens. This was attributed to changes in the NCA unit cell with decreasing Li content [30].

2.3. Calorimetry of 18650s and harvested electrodes

The IBC was calibrated before each use using an Al slug of similar size and mass to the 18650. During each calibration the slug was loaded into the instrument and allowed to equilibrate to the operating temperature (25 °C). Then, 3 W of power was passed through the Al slug and the machine was allowed to equilibrate again. The recorded thermal power and supplied electrical power were compared to set a new baseline. During IBC battery testing, the 18650 was allowed to reach thermal equilibrium before a current was applied. At the start of each charge or discharge step the zero values were compared to the baseline and adjusted accordingly. After each electrochemical step, the cell rested for 4 h to return to thermal equilibrium.

IBC-coupled experimentation enabled the measure of heat flow to and from the cell during operation. Heat generation, $\dot{Q}_T$, after a 4-h rest was taken as thermal equilibrium and set to zero. Integrating heat flow with respect to time yields the total heat generated during operation:

$$Q_T = \int_0^{t_{end}} \dot{Q}_T dt, \tag{11}$$

with Q_T given in joules.

Operando isothermal calorimetry of harvested electrodes was performed using a custom-made calorimeter [55]. Harvested electrodes had an area of 1 cm^2. Testing was performed on three cell configurations: NCA/Li, Graphite + Si/Li, and NCA/Graphite + Si. The instantaneous heat generation at each electrode was calculated based on the heat flux measured by the thermoelectric heat flux sensors (greenTEG, gSKIN-XP) placed behind the target electrode. The heat generation was calculated as:

$$\dot{Q}_i(t) = q_i''(t)A_i = \frac{\Delta V_i(t)}{S_i}A_i \text{ with } i = NCA, Graphite + Si, \text{or } Li \tag{12}$$

where A_i (cm^2) is the area of the electrode, $\Delta V_i(t)$ (μV) is the voltage difference measured by the heat flux sensor, and S_i is the sensitivity of the heat flux sensor (μV/(W/cm^2)). The total heat generation of the cell is the sum of the two electrodes

$$\dot{Q}_T(t) = \dot{Q}_{cathode}(t) + \dot{Q}_{anode}(t) \tag{13}$$

where lithium corresponds to the anode in a half-cell, and Graphite + Si is the anode in a full cell.

Open circuit voltages, U_{OCV}, and entropic potentials, $\partial U_{OCV}/\partial T$, of harvested electrodes were measured in a half-cell coin cell [56]. 30-min C/20 pulses were followed by a 5.5-h relaxation period, with 5 °C changes in temperature between 20 °C and 30 °C in the last 40 min. Analogous to the 18650 full cells, dV/dt analysis was performed on half cells containing recovered electrodes during select entropic potential steps indicated that electrochemical equilibrium was achieved in this time frame, ***Fig. S3***. To ensure thermodynamic equilibrium was reached, the temperature difference between the cold plate and top of the coin cell was verified to be less than 0.1 °C and the time rate of change of the open circuit voltage during relaxation $\partial U_{OCV}/\partial t$ was less than 1 mV/h. C-rates were calculated based on the areal capacity of the full cell, 4.45 mAh/cm^2. Data is presented as a function of SoC with respect to the 18650 cells wherein 0 % SoC indicates that the cathode material is fully lithiated and the anode material is delithiated. As a result, when the harvested anode vs Li cell is fully charged, Li is removed from the harvested anode, but it is presented as 0 % SoC.

3. Results and discussion

3.1. Rate dependent calorimetry of 18650s

Galvanostatic testing of a commercial 18650 cell yielded the expected rate-dependent electrochemical response, Fig. 1. Discharge capacities increased with slower rates from 3.23 to 3.37 Ah, comparable to the manufacturer rated 3.4 Ah. During 1C charge, the cell delivered 2.05 Ah during the CC step and 1.18 Ah during the CV step for a total of 3.23

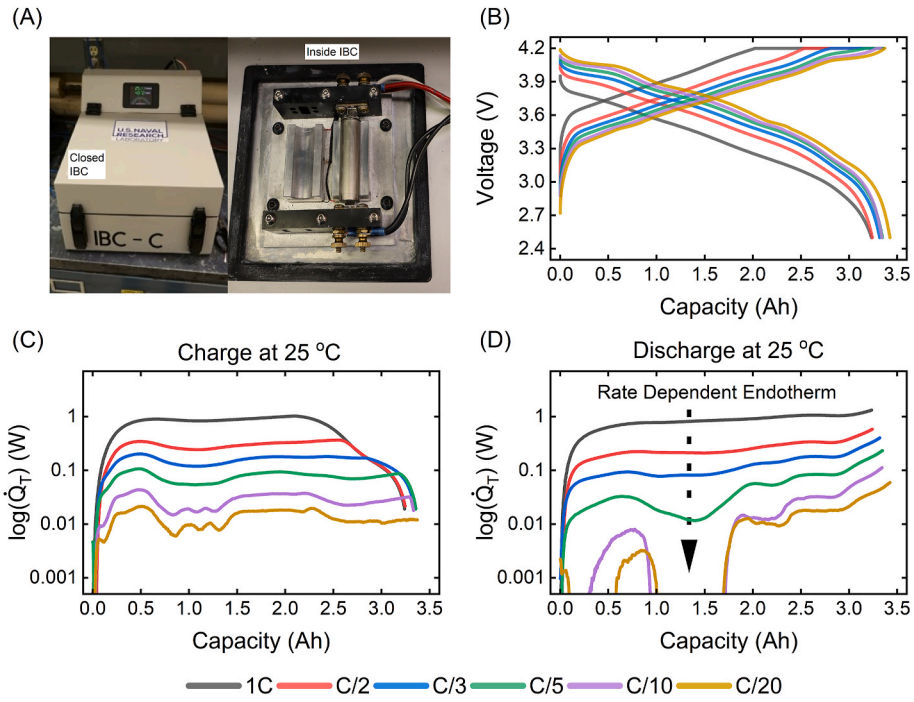

Fig. 1. Isothermal Battery Calorimetry (IBC) testing of a NCA/Graphite + Si 18650 cell. (A) photograph of the closed IBC (left) and open chamber (right). (B) voltage profiles, heat generation profiles on (C) charge and (D) discharge of an 18650 NCA/Graphite + Si cell as a function of C-rate.

Ah. The onset of CV charging corresponded with a rapid decay in the observed current and heat generation, Fig. 1C. Moreover, there were multiple heat generation features that only resolved at C/10 or lower. For example, local maxima in $\dot{Q}_T$ emerged on charge between 0.8 and 1.4 Ah and at ~2.24 Ah. Upon discharge, decreasing C-rates resulted in an endothermic region between 1.0 and 1.75 Ah, Fig. 1D. This endotherm, unnoticeable at C/3, begins to manifest at C/5, and is fully realized during C/10 and C/20 cycling.

These observations highlight the influence of applied current on heat generation and are described through the combination of Equations (1), (2) and (6):

$$\dot{Q}_T \approx \dot{Q}_{rev} + \dot{Q}_J + \dot{Q}_{mix} \approx IT\Delta S + I^2R(x) + \dot{Q}_{mix}\,. \tag{14}$$

$\dot{Q}_J$ will always be exothermic, but $\dot{Q}_{rev}$ may be exothermic or endothermic depending on the direction of the applied current. Therefore, an endothermic feature is only possible if $\dot{Q}_{rev} > \dot{Q}_J + \dot{Q}_{mix}$. This condition is achievable at slow C-rates, like C/10 and C/20, where $\dot{Q}_{mix}$ is negligible and $I > I^2$ (when I < 1). Data visualization was also very influential

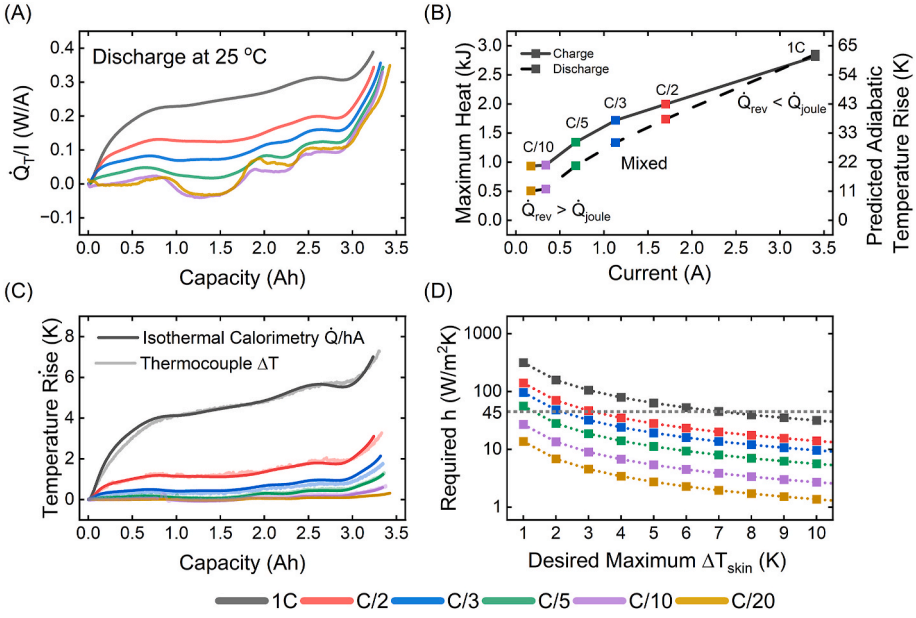

Fig. 2. Predicted and experimental temperature rise of a commercial 18650 NCA/Graphite + Si cell as a function of C-rate. (A) Heat generation normalized by applied current on discharge as a function of C-rate. (B) Maximum heat generated and predicted adiabatic temperature rise. (C) Comparisons between predicted temperature rise when h_{eff} = 45 W/m^{2}K and measured skin temperature increase as a function of c-rate. (D) Required h_{eff} to maintain desired maximum ΔT_{skin} during discharge.

on the interpretation of the heat generation profiles. The log scale presented in Fig. 1 was useful to compare the orders-of-magnitude difference in heat generation but cannot capture the negative values associated with endothermic features.

By normalizing $\dot{Q}_T$ by the applied current (W/A), heat generation rates across C-rates, even during endothermic events, are comparable, Fig. 2A. In fact, $\dot{Q}_T/I$ at C/10 and C/20 were almost identical. This finding was rationalized by revisiting a normalized Equation (14):

$$\dot{Q}_T/I \approx T\Delta S + IR(x) + \dot{Q}_{mix}/I\,. \tag{15}$$

In this form the entropic term and $\dot{Q}_{rev}$ is not influenced by the applied current. Therefore, if the heat generated is dominated by $\dot{Q}_{rev}$, then the magnitude of $\dot{Q}_T/I$ should be constant regardless of C-rate. In other words, when the C-rate is low, $\dot{Q}_{rev} > \dot{Q}_J + \dot{Q}_{mix}$ so that $\dot{Q}_T/I \approx T\Delta S$. This relationship was observed in the case of C/10 and C/20 testing, Fig. 2A. To further investigate this finding, HPPC testing was performed to calculate R_{DC} and $\dot{Q}_J$ as functions of SoC, Fig. S4. $\dot{Q}_T$ and I^2R_{HPPC} are of similar magnitude at C/3 and above. But at lower C-rates, $\dot{Q}_T$ dominates I^2R_{HPPC}, supporting the claim that the observed endotherm is the result of an electrochemical process occurring within the cell. After a wholistic review of the 18650's C-rate performance, heat generation at 1C was deemed to be dominated by the I^2 term in $\dot{Q}_J$. The middle C-rates of C/5, C/3, and C/3 were deemed to be of a mixed domain where both $\dot{Q}_{rev}$ and $\dot{Q}_J$ contribute meaningfully to $\dot{Q}_T$. And lastly, the lower C-rates of C/10 and C/20 were identified as dominated by $\dot{Q}_{rev}$.

Integrating $\dot{Q}_T$ with respect to time yielded Q_T presented in kJ, Fig. 2. Decreasing C-rates reduced the total heat from 2.81 kJ at 1C to 0.96 kJ at C/10 and 0.93 kJ at C/20 on charge. The comparable heat generated at C/10 and C/20, further supports the finding that both of these conditions were $\dot{Q}_{rev}$ dominated. Heat values were lower on discharge at 0.59 kJ and 0.52 kJ for C/10 and C/20, respectively. Q_T increased to 2.85 kJ at 1C, keeping in step with the rate dependence seen on charge. $\dot{Q}_T$ values were also presented as a function of voltage and compared to voltage vs capacity curves, Figure S5, Figure S6, and ***Fig. S7***. Features in the heat vs voltages curves aligned well with plateaus in the capacity vs voltage graphs. This was reflected in the derivatives of the heat vs voltage (dHeat/dV) and in the derivative of the capacity vs voltage (dQ/dV). Peak position and shape of the dHeat/dV and dQ/dV curves correlated across C-rates, further highlighting the interplay between electrochemistry and heat generation. Interestingly, the dHeat/dV and dQ/dV curves deviated in shape from each other above 3.6V during C/20 discharge. In this region, the heat generation profile was endothermic, resulting in a positive dHeat/dV features, whereas the dQ/dV features were negative. But the voltage positions of these features agreed, reaffirming their correlation.

Q_T is understood as the total heat generated by the cell during operation. This heat could either be rejected by the cell into its environment or absorbed by the cell. Highly-insulated cells would experience a greater temperature rise, where the cell absorbs more of the heat generated during operation. Using the 18650's heat capacity, c_p, of 1.014 J/(g*K) at 3.46 V, and the relationship,

$$\Delta T_{adiabatic} = Q_T/(m{*}c_p) \tag{16}$$

Q_T was used to predict the cell's temperature rise under adiabatic conditions, Fig. 2B. The heat generated of 0.96 kJ at C/10 predicted a temperature rise of 11.3 °C. For comparison, the skin temperature ΔT_{skin} changed measured by a thermocouple was only 0.6 °C for cells discharged at C/10 in a climate-controlled chamber with convective cooling from a fan at 25 °C, Fig. S8. These predicted adiabatic values are much higher than thermocouple skin temperature measurements and are intended to approximate the upper limit that a highly insulated cell could experience.

IBC $\dot{Q}_T$ and convection cooled ΔT_{skin} measurements were linked through Equation (8), using an h_{eff} of 45 W/(m^2K), Fig. 2C. This value agrees with h_{eff} of other fan cooled ovens used for temperature-controlled battery testing [57]. By its nature $\dot{Q}_T$ was measured in a highly controlled thermal environment compared to the convective cooled ΔT_{skin} measurements. The good agreement of these two measurements across C-rates indicates that ΔT_{skin} measurements may be able to approximate $\dot{Q}_T$ trends, given a known h value. This relationship was generalized in Fig. 2D to calculate the h_{eff} required to maintain different skin temperature rises as a function of C-rate. At 1C, the h_{eff} to maintain $\Delta T_{skin} < 3°$ is above 100 W/(m^2K) which approaches the upper bounds of cooling achievable by forced air convection [20]. Moreover, more complex scenarios may require the underlying assumptions of equations (8) and (16) to be modified, like cells at the center of a large array being shielded from the cooling system by neighboring cells. In effect, these central cells would have a lower h_{eff}, ultimately experiencing a more adiabatic environment and a larger temperature rise.

3.2. Calorimetry of harvested electrodes

To identify electrode specific calorimetric response, NCA and Graphite + Si electrodes were harvested from the 18650 and used in a custom calorimeter as described in **Section 2.3**. In short, the calorimeter allowed for harvested electrodes to be tested in a full cell configuration while the heat generation at each electrode to be recorded. [55]$\dot{Q}_T$ in mW/cm^2 during galvanostatic testing at C/2 for the harvested electrodes and for an 18650 is reported in Fig. 3. Harvested electrodes were also tested vs Li electrodes, where $\dot{Q}_T$ was consistent across electrode configuration, further supporting that the custom calorimetric isolates the heat generated by each electrode, not from the cell as a whole, Fig. S9. During charging, Fig. 3a, the heat generation rates were relatively constant for both electrodes at around 0.4 mW/cm^2 for the harvested cathode and 0.1 mW/cm^2 for the harvested anode. By contrast, during discharging, the harvested anode's heat generation increased continuously to 0.8 mW/cm^2 while the harvested cathode hovered around −0.1 mW/cm^2. Heat generation was higher during delithiation (cathode on charge and anode on discharge), than lithiation, a phenomenon attributed to a thermal penalty associated with the solvation of Li ions as they are released from the electrode into the electrolyte [7]. Interpretation of the 18650's C/2 calorimetry, Fig. 2, placed C/2 testing at the higher end of the mixed domain where both $\dot{Q}_{rev}$ and $\dot{Q}_J$ contribute meaningfully to $\dot{Q}_T$. The harvested electrode calorimetry adds nuance to this discussion through evidence that additional heat generation sources, like solvation, manifest at C/2.

Normalizing heat generation by the electrode surface area allowed for a more even comparison between the 18650 and the 1 cm^2 electrode used in the custom calorimeter. Overall, the magnitude of heat generation was comparable across form factors, especially during discharge, confirming the accuracy and precision of the custom-made calorimeter with regard to the commercial IBC testing of 18650s. The discrepancy on charge could be rationalized through a difference in SoC, and reversible heat generation, and prompted further electrochemical investigation of this system and will be discussed in later sections.

3.3. ΔS measurements of 18650 and harvested electrodes

ΔS (mV/K) and U_{OCV}, measurements of commercial 18650s and recovered electrodes in Li half-cell coin cells are presented in Fig. 4 and Figure S8**.** Data is presented in terms of SoC, with 4.49 mAh/cm^2 corresponding to 100 % SoC for the full cell. During full cell charge, the cathode's active material (NCA) is delithiated while the anode's active material (Graphite + Si) is lithiated. This corresponds to the data presented in Fig. 4a, b, 4c, and Figure S8 and should be read left-to-right. During full cell discharge, the electrochemical processes are reversed as the NCA cathode is lithiated and the Graphite + Si anode is

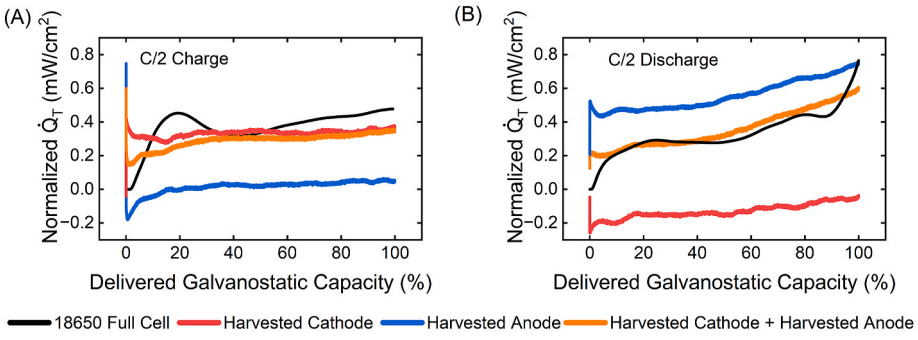

Fig. 3. Isothermal calorimetry testing of recovered electrodes during (A) C/2 charge and (B) C/2 discharge at 25 °C. $\dot{Q}_T$ is normalized by the electrode area, while capacity is normalized to the capacity delivered during galvanostatic electrochemistry.

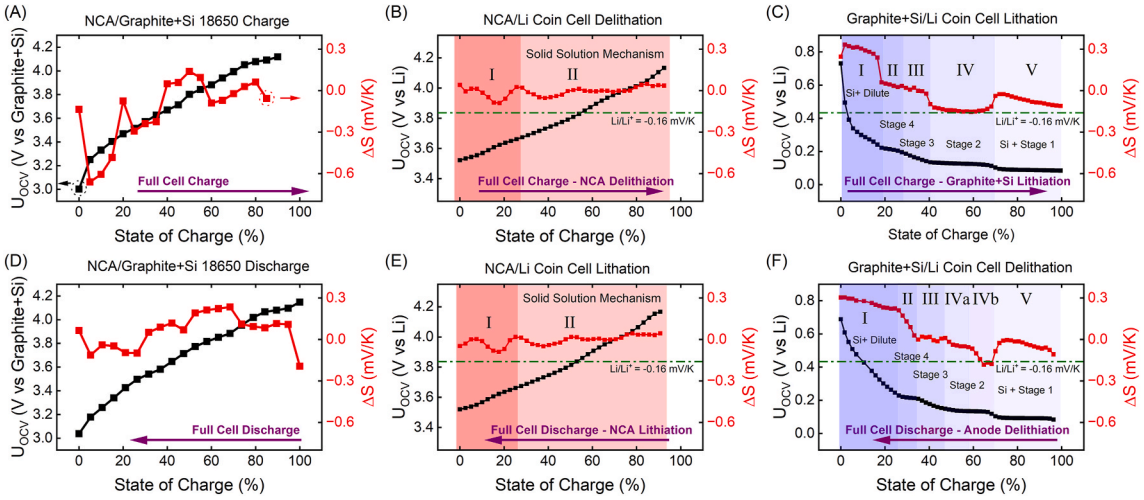

Fig. 4. Rest potential and entropic potentials of an NCA/Graphite + Si 18650 full cell and harvested electrode/Li coin cells. (A) Charge of an NCA/Graphite + Si 18650 full cell at C/10. (B) Charge of an NCA/Li coin cell at C/10. (C) Charge of a Graphite + Si/Li coin cell at C/20. (D) Discharge of an NCA/Graphite + Si 18650 full cell at C/10. (E) Discharge of an NCA/Li coin cell at C/10. (F) Discharge of a Graphite + Si/Li coin cell at C/10. State of Charge is in reference to the full cell and was determined by areal capacities (4.49 mAh/cm^2). Black and red lines denote rest potentials and entropic potentials, respectively. The entropy of Li/Li$^+$, −0.16 mV/K, is indicated as a green line in panels B,C,E, and F. (For interpretation of the references to colour in this figure legend, the reader is referred to the Web version of this article.)

delithiated. Discharge data, Fig. 4d, E, 4F, and Figure S8**,** should be read right-to-left, as discharge begins at 100 % SoC.

In the commercial 18650 cell, the rest potentials showed good agreement across charge and discharge processes, indicating that Δ*S* measurements were taken at similar SoCs and thermodynamic conditions. Full cell $\Delta S_{NCA/graphite+Si}$ values started negative at low SoCs before increasing and turning positive around 40 % SoC. Δ*S* values were larger on discharge than charge at all points except at 20 and 100 % SoC, resulting in a hysteresis between $\Delta S_{18650\ discharge}$ and $\Delta S_{18650\ charge}$, Fig. S10. This finding suggests a path-dependent reaction and mirrors entropic studies of the NCA/Graphite + Si system by Wojtala et al. [44]

For the delithiation of the recovered NCA/Li coin cell, Δ*S* measurements were separated into two main regions, Fig. 4B and E. Region I showed an increasing open circuit voltage, accompanied by a concave up ΔS. This trend in ΔS has sometimes been associated with an insulator to metal, or semiconductor to metal transition [7]. Indeed, materials similar to NCA, like lithium cobalt oxide do exhibit this transition. However, to the best of our knowledge, NCA does not go through this transition. Instead, the local minimum in ΔS at ~20 % SoC was attributed to two factors: 1) the configuration entropy between Li-ions and vacant Li-ion sites in the interlayer of the NCA crystal, with similar findings reported for the lithiation of $LiCoO_2$,[58] and 2) a decrease in charge transfer resistance [59]. Region II consisted of increasing U_{OCV} and steady ΔS values that hovered around 0 mV/K. A constant ΔS value as a function of SoC indicates that the (de)lithiation of NCA follows a solid solution mechanism [8]. Moreover, these values were taken with respect to Li metal. As outlined by Kang et al. [45], the entropic potential of the active material in a Li metal coin cell can be calculated by using S_{Li} = ~15.7 J/(mol*K) at standard conditions, or in this case −0.16 mV/K. Therefore, an entropic potential of 0 mV/K indicates that the entropy of the NCA active material is approximately 0.16 mV/K. This finding is in agreement with diffraction studies that report a solid-solution mechanism of NCA for all Li contents explored in this work [60]. The harvested NCA/Li half-cell also exhibited minimal voltage hysteresis and the same two regions were also identified were on lithiation, confirming the high reversibility of lithium (de)insertion in NCA, Fig. 4E.

On the anode side, the harvested Graphite + Si/Li coin cell displayed both voltage and entropic hysteresis. In contrast to the three ΔS regions presented by Baek et al., for the Graphite/Li system [8], five distinct entropic potential regions were identified during Graphite + Si/Li lithiation. Each ΔS region was associated with either Si redox or a stage of graphite lithiation: dilute, stage 4 ($Li_{0.1}C_6$), stage 3 ($Li_{0.2}C_6$), stage 2 ($Li_{0.5}C_6$), stage 1 (LiC_6) [37]. There are sharp drops in Δ*S* at the boundaries of each of these regions indicating a first-order phase transition. In region I, U_{OCV} was over 0.2 V and both U_{OCV} and ΔS were decreasing, Fig. 4C. It has been shown that in an electrode made of graphite and silicon, only silicon is electrochemically active above 0.2 V

[61]. Therefore, ΔS was assigned to Si redox and the dilute phase of graphite. In region II, the entropic potential exhibited a sharp drop which could be due to the beginning of lithiation of the graphite particles. Furthermore, the open circuit voltage displayed a short plateau, corresponding with the first order phase transition between the dilute phase and stage 4 ($Li_{0.1}C_6$) [37]. In region III, both the open circuit voltage and entropic potential were decreasing. It is believed that during region III both silicon and graphite were being lithiated, and graphite transitioned from stage 4 ($Li_{0.1}C_6$) to stage 3 ($Li_{0.2}C_6$). Region IV exhibited a plateau in both U_{OCV} and ΔS attributed to transition from graphite Stage 3 ($Li_{0.2}C_6$) to stage 2 ($Li_{0.5}C_6$). The staging reactions of graphite occur with two-phases coexisting, during which the entropic potential was expected to remain constant [8]. This is not the case in Region V, where the sloping ΔS was attributed to both the reaction between graphite stage 2 ($Li_{0.5}C_6$) to stage 1 (LiC_6) and the lithiation of Si below 0.05V.

Delithiation of the harvested anodes, Fig. 4F, largely followed the reverse trends of lithation, albeit with the addition of a sixth region. Discharge started with region V, attributed to the reverse delithiation of Si and graphite stage 1 (LiC_6) to stage 2 ($Li_{0.5}C_6$). Region IV was separated in to IVa and IVb because the ΔS showed two distinct magnitudes over the same U_{OCV} plateau. Regions IVa and IVb was still attributed to the transition from graphite stage 2 ($Li_{0.5}C_6$) to stage 3 ($Li_{0.2}C_6$), but the rise in ΔS between regions V and IV was attributed to the presence of silicon. Region III exhibited increasing ΔS and U_{OCV} associated with a Graphite stage 3 ($Li_{0.2}C_6$) to stage 4 ($Li_{0.1}C_6$) transition. In region II, the open circuit voltage exhibited a short plateau, corresponding to the first order phase transformation between stage 4 and the dilute phase [37]. Finally, in region I, both U_{OCV} and ΔS increased, corresponding to lithium deintercalation in a solid solution. In region I, the dilute phase of graphite cannot be delithiated farther, therefore, most of the behavior was attributed to Si redox.

The graphite half-cell displayed a hysteresis in its ΔS, ***Fig. S10***. Previous reports indicate a preference towards Si during the lithation of Graphite + Si electrodes [61]. Additionally, Uxa et al. has reported that amorphous Si electrodes (de)lithiates heterogeneously via Li-poor and Li-rich intermediary phases, with Li ions being irreversibly trapped in the Li-poor phase during delithiation [62]. Similar reports of poor delithiation kinetics of Graphite + Si electrodes have shown Li accumulation within Si particles overtime leading to high energy barriers and inhomogeneous reaction pathways during discharge [63,64]. We believe that the hysteresis of the Graphite + Si electrode's ΔS may be explained by path dependent reactions.

3.4. Reconstruction of 18650's C/10 heat generation profiles

Half-cell entropic potentials were used to reconstruct full cell entropic potentials according to: $\Delta S_{NCA/Graphite+Si} = \Delta S_{NCA/Li} - \Delta S_{Graphite+Si/Li}$, and presented as a function of SoC, Fig. 5. $\Delta S_{NCA/Graphite+Si}$ measurements ranged from −0.6 to 0.2 mV/K and were larger in magnitude than $\Delta S_{NCA/Li}$ or $\Delta S_{Graphite\ +\ Si/Li}$. This was rationalized through Equation (5), which implies entropic potential measurements are taken at a constant pressure. Differences in pressure between the coin cell and 18650 form factors have been reported [65], and may account for the differences in the magnitude of ΔS. Pressure differentials can develop within an 18650 jelly roll during cycling [66,67], further muddling the comparison between full cell 18650 and harvested electrodes in coin cells. Additionally, it should be reiterated that the ΔS measurements of recovered electrodes are taken with respect to Li and therefore encompass the entropy of Li in the measurement.

Still, there was good agreement between the shape and features of the reconstruction and full cell curves. In this way, the regions of the full cell's $\Delta S_{NCA/Graphite+Si}$ curve could be associated with specific electrode specific phenomena as presented in Fig. 4. Specifically, at low SoC, the $\Delta S_{NCA/Graphite+Si}$ correlated to the Si + Dilute domain, and the region of the discharge endotherm 55–85 % SoC, tracked well with the Graphite stage 2 domain. Overall, the NCA electrode experienced little change in ΔS during (de)lithiation compared to the graphite/Si electrode, indicating that the entropic changes in the full cell are due in majority to the anode.

A two-component reconstruction of $\dot{Q}_T$ using $\dot{Q}_{rev} + \dot{Q}_J$, was developed by applying Equations (2) and (6) to the ΔS measurements and electrochemical data taken during the entropic potential measurements of 18650 cell, Fig. S9. Similar to the entropic potential reconstructions, this two-component reconstruction of $\dot{Q}_T$ was divided into different domains based on the anode staging. On discharge, the $\dot{Q}_{rev} + \dot{Q}_J$ reconstruction was able to capture the discharge endotherm and the large increase in heat generation at low SoCs, Fig. 6. The endotherm was correlated to the large ΔS values in $\dot{Q}_{rev}$ associated with the stage 2 phase transition in the graphite anode. The large increase in heat generation at the end of the discharge was attributed to $\dot{Q}_J$ due to large overpotentials observed during NCA lithiation and Graphite + Si delithiation at the low SoC region, Fig. 1B. Moreover, skin temperature measurements agreed with $\dot{Q}_T$ and the two-component reconstruction when $h_{eff} = 45\ W/m^2K$.

On charge, the reconstruction exhibited good agreement between the IBC data, skin temperature measurements, and ΔS features correlated with the staging identified anode-side domains. The two-component reconstruction, however, could not capture the exothermic feature at 15 % SoC, with $\dot{Q}_{rev,cathode}$ and $\dot{Q}_{rev,anode}$ both predicting an endothermic response larger than $\dot{Q}_J$. The two-component reconstruction uses measurements taken at rest to predict the operando $\dot{Q}_T$. The large

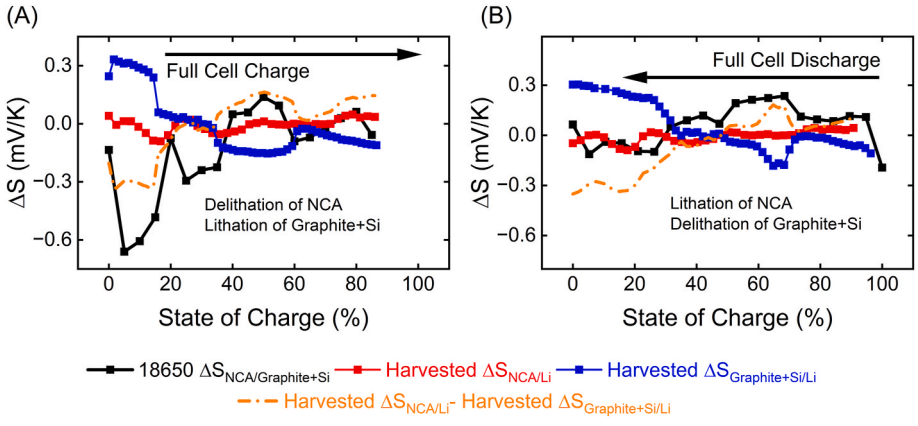

Fig. 5. Full cell/half-cell reconstruction of entropic potentials on (A) charge and (B) discharge. The reconstruction (orange) was made by subtracting ΔS_{anode} (blue) from $\Delta S_{cathode}$ (red). (For interpretation of the references to colour in this figure legend, the reader is referred to the Web version of this article.)

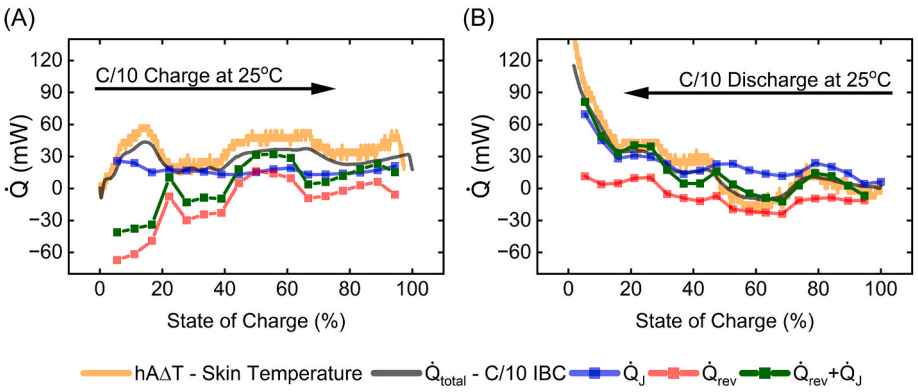

Fig. 6. Comparison of IBC, modified skin temperature, and two-component reconstruction ($\dot{Q}_{rev}+\dot{Q}_J$) of during C/10 (A) charge and (D) discharge for a 18650 full cell. State of Charge was determined by areal capacities of the 18650 (4.49 mAh/cm^2).

disagreement between the two methods below 20 % SoC on charge suggests that another heat generation source is present during operation that cannot be accounted for.

To probe the possibility of operando effects not captured by the two-component reconstruction, IBC coupled GITT testing collected heat generation, $\dot{Q}_{GITT}$, in 5 % SoC intervals, corresponding to each ΔS interval to compare to the continuously collected $\dot{Q}_T$, Fig. 7. Upon initial inspection, an initial endotherm was observed at the start of continuous IBC testing and during GITT step 1, that was mitigated as the system entered steady state redox. Upon the application of a current, the same endothermic feature returned for the first four GITT charge steps before $\dot{Q}_{GITT}$ matched $\dot{Q}_T$. Concurrently, there were stark disagreements between the galvanostatic and GITT voltage profiles at analogous total capacities, Fig. 7A insert. Therefore, the endothermic difference between GITT and galvanostatic heat generation profiles was attributed to the energy the cell must absorb to overcome to overcome $\eta_{activation}$ at the start of each GITT step. The difference in heat generated continuously collected $\dot{Q}_T$ and intermittent $\dot{Q}_{GITT}$ was deemed the activation energy, according to:

$$\Delta Q = \int_{t_{GITT,step,start}}^{t_{GITT,step,end}} \dot{Q}_{Galvano} - \dot{Q}_{GITT} dt. \tag{17}$$

On discharge, ΔQ hovered between −20 and 20 J, suggesting more favorable kinetics during the spontaneous discharge process. ΔQ was largest during the start of charge, peaking at ~50 J at 20 % and then again at 70 % SoC.

These two points corresponded to the end of the Si + Dilute and Graphite stage 2 domains, respectively, suggesting prolonged kinetic

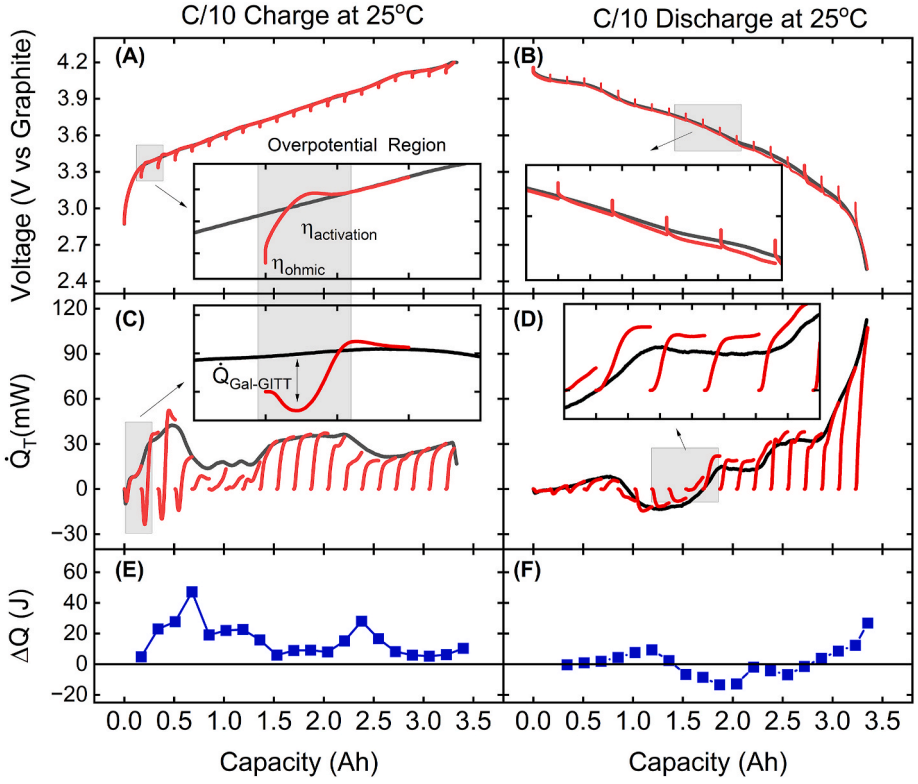

Fig. 7. IBC coupled GITT testing for an NCA/Graphite + Si 18650. (A, B) Voltage response during continuous and intermittent testing. (C, D) Heat generation during continuous and intermittent testing. (E, F) ΔQ on charge and discharge. Continuous galvanostatic testing and GITT testing are shown in black and red, respectively. All testing was performed at C/10 at 25 °C under isothermal conditions. (For interpretation of the references to colour in this figure legend, the reader is referred to the Web version of this article.)

limitations at lower SoC and during phase transitions [68]. At the beginning of charge, the cathode is fully lithiated. Operando synchrotron XRD studies have shown that while reaction heterogeneity due to surface impurities are possible, NCA should react as a solid solution up to 4.1V vs Li [60]. Moreover, Li ion diffusivity measurements through micron sized NCA are sufficient to ensure bulk transport at all SoC [69]. At the same time, the anode starts accepting lithium and should undergo a phase transformation from the dilute to stage 3 (LiC_{18}) phase. Li diffusion through graphite has been reported to be two order of magnitude slower at low Li contents (~LiC_{36}) than higher Li contents [70]. More interestingly, Graphite + Si anodes have been shown to (de) lithiate heterogeneously. Berhaut et al. [71] reported uniform lithiation of graphite throughout the thickness of a Graphite + Si electrode, while Si particles closer to the electrode/electrolyte interface have higher Li contents than Si particles away from the interface during operation. They also reported evidence of phase-to-phase redistribution of Li throughout the electrode during periods of relaxation.

The SoCs with the largest disagreement between $\dot{Q}_T$ and the two-component reconstruction were associated with the largest ΔQ values, Fig. 7. Therefore, we postulate that ΔQ can serve as proxy for kinetic influences like $\dot{Q}_{mix}$, a value for which direct measurement remains elusive. All this in tandem, we attribute the mismatch between $\dot{Q}_T$ and the two-component reconstruction to discrepancies between the rest state and active state of the system as described by ΔQ. Moreover, $\dot{Q}_{rev}$ or $\dot{Q}_J$ ultimately rely on equilibrium potentials and therefore cannot capture kinetic effects that can be observed during operando calorimetry.

4. Conclusion

Herein, we present the thermo-electrochemical characterization of a commercial 18650 NCA/Graphite + Si Li-ion cell. The larger form factor and active mass of the 18650 compared to coin cells allowed for precise heat flow calorimetry even at low C-rates. ΔS measurements of recovered electrodes in Li half cells were used to fingerprint heat generation features with electrode-specific phenomena. The NCA cathode was shown to have entropic potential values hovering around 0 mV/K, suggesting a solid solution mechanism at all SoCs. On the other hand, ΔS_{anode} was highly path dependent, varying greatly as a function of SoC and charge or discharge condition. Still, the discharge endotherm observed at low C-rate cycling fingerprinted to the stage 3 and stage 2 delithiation of graphite in the anode.

IBC coupled electrochemical testing was used to deconstruct $\dot{Q}_T$ into its constituent sources of $\dot{Q}_{rev}$ and $\dot{Q}_J$. There were electrochemical conditions (C-rate, SoC, charge or discharge) where each of these heat generation sources contributed meaningfully to $\dot{Q}_T$. $\dot{Q}_J$ accounted for most of the heat generation at 1C, while the middle conditions of C/2, C/3, and C/5 exhibited mixed domains of heat generation. Heat generation rates at C/10 and C/20 were similar in magnitude and therefore correlated to $\dot{Q}_{rev}$ dominated heat generation. Integrating $\dot{Q}_T$ with respect to time, yielded Q_T in J, or the total heat generated during operation with the 18650 generated between 0.94 kJ (C/20) to 2.7 kJ (1C) on charge. Using these values, heat capacity calculations predicted that the cell generates enough heat at 1C to increase from 25 °C to 82 °C under adiabatic conditions. By contrast, an increase of only 7.5 °C was observed at 1C when cycled in a fan-controlled chamber. These findings allude to the fact while the total energy generated by the cell is C-rate dependent, cell temperature rise is environment dependent. Galvanostatic IBC data was also compared with IBC data taken during intermittent operation. The difference in heat generation between galvanostatic and GITT IBC data, ΔQ, correlated with the largest discrepancy between $\dot{Q}_T$ and the $\dot{Q}_{rev} + \dot{Q}_J$ reconstruction at low SoC (<20 %) on charge. This finding suggest that a large amount of heat generated at low SoCs on charge is due to kinetic factors (e.g. a crystallographic phase change in the NCA cathode material) and cannot be captured by $\dot{Q}_{rev} + \dot{Q}_J$ measurements made at rest.

The presented thermo-electrochemical approach is a valuable tool in identifying electrode-specific contributions at various SoCs and C-rates. Areas of interest for future studies include applying a thermo-electrochemical approach in conjunction with a computational model and/or tracking the evolution of $\dot{Q}_T$ as cells undergo degradation and aging, with phenomena of interest including the relative capacity degradation of the Si and graphite phase of the anode, the buildup of resistive electrode-electrolyte interface layers, the loss of lithium inventory, and cracking of cathode active particles. While the electrochemical signatures of these mechanisms have been extensively studied, their impacts on heat generation and the thermal management of commercial systems built of many thousands of cells, has not yet been explored. Ultimately, this work combined IBC testing, skin temperature measurements, and entropic potential experiments into a rigorous thermo-electrochemical characterization of the NCA/Graphite + Si system.

CRediT authorship contribution statement

Patrick J. West: Writing – review & editing, Writing – original draft, Visualization, Methodology, Investigation, Formal analysis, Data curation, Conceptualization. **Nicolas Leport:** Writing – review & editing, Visualization, Formal analysis, Data curation. **Dillon Hayman:** Visualization, Data curation. **Rachel Carter:** Writing – review & editing, Conceptualization. **Corey T. Love:** Writing – review & editing, Resources, Conceptualization. **Laurent Pilon:** Writing – review & editing, Supervision, Resources, Methodology, Funding acquisition, Data curation. **Gordon H. Waller:** Writing – review & editing, Supervision, Resources, Project administration, Methodology, Funding acquisition, Formal analysis, Conceptualization.

Declaration of competing interest

The authors declare that they have no known competing financial interests or personal relationships that could have appeared to influence the work reported in this paper.

Acknowledgements

NL and LP acknowledge the support of the Center for Synthetic Control Across Length-scales for Advancing Rechargeables (SCALAR), an Energy Frontier Research Center funded by the U.S. Department of Energy, Office of Science, Basic Energy Sciences under Award #DE-SC0019381. PJW, DH, RC, CTL, and GHW acknowledge the support of the Naval Sea Systems Command (NAVSEA). PJW was supported through an American Society for Engineering Education (ASEE) post-doctoral program.

Appendix A. Supplementary data

Supplementary data to this article can be found online at https://doi.org/10.1016/j.jpowsour.2024.236044.

Data availability

The authors do not have permission to share data.

References

[1] V. Muenzel, A.F. Hollenkamp, A.I. Bhatt, J. de Hoog, M. Brazil, D.A. Thomas, I. Mareels, A comparative testing study of commercial 18650-format lithium-ion battery cells, J. Electrochem. Soc. 162 (8) (2015) A1592, https://doi.org/10.1149/2.0721508jes.

[2] Y. Gao, Z. Pan, J. Sun, Z. Liu, J. Wang, High-energy batteries: beyond lithium-ion and their long road to commercialisation, Nano-Micro Lett. 14 (1) (2022) 94, https://doi.org/10.1007/s40820-022-00844-2.

[3] F. Leng, C.M. Tan, M. Pecht, Effect of temperature on the aging rate of Li ion battery operating above room temperature, Sci. Rep. 5 (1) (2015) 12967, https://doi.org/10.1038/srep12967.

[4] W. Shen, N. Wang, J. Zhang, F. Wang, G. Zhang, Heat generation and degradation mechanism of lithium-ion batteries during high-temperature aging, ACS Omega 7 (49) (2022) 44733–44742, https://doi.org/10.1021/acsomega.2c04093.

[5] C.D. Quilty, P.J. West, W. Li, M.R. Dunkin, G.P. Wheeler, S. Ehrlich, L. Ma, C. Jaye, D.A. Fischer, E.S. Takeuchi, et al., Multimodal electrochemistry coupled microcalorimetric and X-ray probing of the capacity fade mechanisms of Nickel rich NMC – progress and outlook, Phys. Chem. Chem. Phys. 24 (19) (2022) 11471–11485, https://doi.org/10.1039/D1CP05254C.

[6] F. Friedrich, T. Zünd, A. Hoefling, J. Tübke, H.A. Gasteiger, Classification of heat evolution terms in Li-ion batteries regarding the OCV hysteresis in a Li- and Mn-rich NCM cathode material in comparison to NCA, J. Electrochem. Soc. 169 (4) (2022) 040547, https://doi.org/10.1149/1945-7111/ac6541.

[7] S.W. Baek, M.B. Preefer, M. Saber, K. Zhai, M. Frajnković, Y. Zhou, B.S. Dunn, A. Van der Ven, R. Seshadri, L. Pilon, Potentiometric entropy and operando calorimetric measurements reveal fast charging mechanisms in PNb9O25, J. Power Sources 520 (2022) 230776, https://doi.org/10.1016/j.jpowsour.2021.230776.

[8] S.W. Baek, M. Saber, A. Van der Ven, L. Pilon, Thermodynamic analysis and interpretative guide to entropic potential measurements of lithium-ion battery electrodes, J. Phys. Chem. C 126 (14) (2022) 6096–6110, https://doi.org/10.1021/acs.jpcc.1c10414.

[9] L.J. Krause, L.D. Jensen, J.R. Dahn, Measurement of parasitic reactions in Li ion cells by electrochemical calorimetry, J. Electrochem. Soc. 159 (7) (2012) A937, https://doi.org/10.1149/2.021207jes.

[10] L.B. Diaz, A. Hales, M.W. Marzook, Y. Patel, G. Offer, Measuring irreversible heat generation in lithium-ion batteries: an experimental methodology, J. Electrochem. Soc. 169 (3) (2022) 030523, https://doi.org/10.1149/1945-7111/ac5ada.

[11] R. Srinivasan, B.G. Carkhuff, Empirical analysis of contributing factors to heating in lithium-ion cells: anode entropy versus internal resistance, J. Power Sources 241 (2013) 560–566, https://doi.org/10.1016/j.jpowsour.2013.04.108.

[12] G.A. Giffin, The role of concentration in electrolyte solutions for non-aqueous lithium-based batteries, Nat. Commun. 13 (1) (2022) 5250, https://doi.org/10.1038/s41467-022-32794-z.

[13] J. Zhou, D. Danilov, P.H.L. Notten, A novel method for the in situ determination of concentration gradients in the electrolyte of Li-ion batteries, Chem. Eur J. 12 (27) (2006) 7125–7132, https://doi.org/10.1002/chem.200600193.

[14] G. Zhang, C.E. Shaffer, C.-Y. Wang, C.D. Rahn, Effects of non-uniform current distribution on energy density of Li-ion cells, J. Electrochem. Soc. 160 (11) (2013) A2299, https://doi.org/10.1149/2.061311jes.

[15] L. Li, J. Chen, H. Huang, L. Tan, L. Song, H.-H. Wu, C. Wang, Z. Zhao, H. Yi, J. Duan, T. Dong, Role of residual Li and oxygen vacancies in Ni-rich cathode materials, ACS Appl. Mater. Interfaces 13 (36) (2021) 42554–42563, https://doi.org/10.1021/acsami.1c06550.

[16] Y. Guo, X. Li, H. Guo, Q. Qin, Z. Wang, J. Wang, G. Yan, Visualization of concentration polarization in thick electrodes, Energy Storage Mater. 51 (2022) 476–485, https://doi.org/10.1016/j.ensm.2022.07.007.

[17] M. Weiss, R. Ruess, J. Kasnatscheew, Y. Levartovsky, N.R. Levy, P. Minnmann, L. Stolz, T. Waldmann, M. Wohlfahrt-Mehrens, D. Aurbach, et al., Fast charging of lithium-ion batteries: a review of materials aspects, Adv. Energy Mater. 11 (33) (2021) 2101126, https://doi.org/10.1002/aenm.202101126.

[18] D. Chalise, W. Lu, V. Srinivasan, R. Prasher, Heat of mixing during fast charge/discharge of a Li-ion cell: a study on NMC523 cathode, J. Electrochem. Soc. 167 (9) (2020) 090560, https://doi.org/10.1149/1945-7111/abaf71.

[19] L.E. Downie, S.R. Hyatt, A.T.B. Wright, J.R. Dahn, Determination of the time dependent parasitic heat flow in lithium ion cells using isothermal microcalorimetry, J. Phys. Chem. C 118 (51) (2014) 29533–29541, https://doi.org/10.1021/jp508912z.

[20] F. Incropera, D. Dewitt, Fundamentals of Heat and Mass Transfer, John Wiley & Sons, Inc., 1996.

[21] A. Hales, L.B. Diaz, M.W. Marzook, Y. Zhao, Y. Patel, G. Offer, The cell cooling coefficient: a standard to define heat rejection from lithium-ion batteries, J. Electrochem. Soc. 166 (12) (2019) A2383, https://doi.org/10.1149/2.0191912jes.

[22] The absolute electrode potential: an explanatory note (Recommendations 1986), J. Electroanal. Chem. Interfacial Electrochem. 209 (2) (1986) 417–428, https://doi.org/10.1016/0022-0728(86)80570-8.

[23] A.J. Bard, L.R. Faulkner, H.S. White, Electrochemical Methods: Fundamentals and Applications, Wiley, 2022.

[24] W. Liu, P. Oh, X. Liu, M.-J. Lee, W. Cho, S. Chae, Y. Kim, J. Cho, Nickel-rich layered lithium transition-metal oxide for high-energy lithium-ion batteries, Angew. Chem. Int. Ed. 54 (15) (2015) 4440–4457, https://doi.org/10.1002/anie.201409262.

[25] P.J. West, C.D. Quilty, Z. Wang, S.N. Ehrlich, L. Ma, C. Jaye, D.A. Fischer, X. Tong, A.M. Kiss, E.S. Takeuchi, et al., Degradation in Ni-rich $LiNi_{1-x-y}Mn_xCo_yO_2$/Graphite batteries: impact of charge voltage and Ni content, J. Phys. Chem. C 127 (15) (2023) 7054–7070, https://doi.org/10.1021/acs.jpcc.2c08971.

[26] D. Carlier, A. Van der Ven, C. Delmas, G. Ceder, First-principles investigation of phase stability in the O2-$LiCoO_2$ system, Chem. Mater. 15 (13) (2003) 2651–2660, https://doi.org/10.1021/cm030002t.

[27] H.-H. Ryu, K.-J. Park, C.S. Yoon, Y.-K. Sun, Capacity fading of Ni-rich Li $[Ni_xCo_yMn_{1-x-y}]O_2$ ($0.6 \leq x \leq 0.95$) cathodes for high-energy-density lithium-ion batteries: bulk or surface degradation? Chem. Mater. 30 (3) (2018) 1155–1163, https://doi.org/10.1021/acs.chemmater.7b05269.

[28] K.D.R. Ekawati, A.P. Sholikah, C.S. Yudha, H. Widiyandari, A. Purwanto, Comparative study of NCA cathode material synthesis methods towards their structure characteristics, in: 2018 5th International Conference on Electric Vehicular Technology (ICEVT), 30-31 Oct. 2018, 2018, pp. 57–61, https://doi.org/10.1109/ICEVT.2018.8628433.

[29] P.-C. Tsai, B. Wen, M. Wolfman, M.-J. Choe, M.S. Pan, L. Su, K. Thornton, J. Cabana, Y.-M. Chiang, Single-particle measurements of electrochemical kinetics in NMC and NCA cathodes for Li-ion batteries, Energy Environ. Sci. 11 (4) (2018) 860–871, https://doi.org/10.1039/C8EE00001H.

[30] M. Guilmard, C. Pouillerie, L. Croguennec, C. Delmas, Structural and electrochemical properties of LiNi0.70Co0.15Al0.15O2, Solid State Ionics 160 (1) (2003) 39–50, https://doi.org/10.1016/S0167-2738(03)00106-1.

[31] H.-H. Ryu, N.-Y. Park, J.H. Seo, Y.-S. Yu, M. Sharma, R. Mücke, P. Kaghazchi, C. S. Yoon, Y.-K. Sun, A highly stabilized Ni-rich NCA cathode for high-energy lithium-ion batteries, Mater. Today 36 (2020) 73–82, https://doi.org/10.1016/j.mattod.2020.01.019.

[32] G.W. Nam, N.-Y. Park, K.-J. Park, J. Yang, J. Liu, C.S. Yoon, Y.-K. Sun, Capacity fading of Ni-rich NCA cathodes: effect of microcracking extent, ACS Energy Lett. 4 (12) (2019) 2995–3001, https://doi.org/10.1021/acsenergylett.9b02302.

[33] J. Zhu, Y. Wang, Y. Huang, R. Bhushan Gopaluni, Y. Cao, M. Heere, M. J. Mühlbauer, L. Mereacre, H. Dai, X. Liu, et al., Data-driven capacity estimation of commercial lithium-ion batteries from voltage relaxation, Nat. Commun. 13 (1) (2022) 2261, https://doi.org/10.1038/s41467-022-29837-w.

[34] D. Matras, T.E. Ashton, H. Dong, M. Mirolo, I. Martens, J. Drnec, J.A. Darr, P. D. Quinn, S.D.M. Jacques, A.M. Beale, A. Vamvakeros, Emerging chemical heterogeneities in a commercial 18650 NCA Li-ion battery during early cycling revealed by synchrotron X-ray diffraction tomography, J. Power Sources 539 (2022) 231589, https://doi.org/10.1016/j.jpowsour.2022.231589.

[35] A.J. Crawford, Q. Huang, M.C.W. Kintner-Meyer, J.-G. Zhang, D.M. Reed, V. L. Sprenkle, V.V. Viswanathan, D. Choi, Lifecycle comparison of selected Li-ion battery chemistries under grid and electric vehicle duty cycle combinations, J. Power Sources 380 (2018) 185–193, https://doi.org/10.1016/j.jpowsour.2018.01.080.

[36] Q. Liu, S. Li, S. Wang, X. Zhang, S. Zhou, Y. Bai, J. Zheng, X. Lu, Kinetically determined phase transition from stage II (LiC_{12}) to stage I (LiC_6) in a graphite anode for Li-ion batteries, J. Phys. Chem. Lett. 9 (18) (2018) 5567–5573, https://doi.org/10.1021/acs.jpclett.8b02750.

[37] J.R. Dahn, Phase diagram of Li_xC_6, Phys. Rev. B 44 (17) (1991) 9170–9177, https://doi.org/10.1103/PhysRevB.44.9170.

[38] J. Asenbauer, T. Eisenmann, M. Kuenzel, A. Kazzazi, Z. Chen, D. Bresser, The success story of graphite as a lithium-ion anode material – fundamentals, remaining challenges, and recent developments including silicon (oxide) composites, Sustain. Energy Fuels 4 (11) (2020) 5387–5416, https://doi.org/10.1039/D0SE00175A.

[39] T. Chen, J. Wu, Q. Zhang, X. Su, Recent advancement of SiOx based anodes for lithium-ion batteries, J. Power Sources 363 (2017) 126–144, https://doi.org/10.1016/j.jpowsour.2017.07.073.

[40] S. He, S. Huang, S. Wang, I. Mizota, X. Liu, X. Hou, Considering critical factors of silicon/graphite anode materials for practical high-energy lithium-ion battery applications, Energy & Fuels 35 (2) (2021) 944–964, https://doi.org/10.1021/acs.energyfuels.0c02948.

[41] M.K.Y. Chan, C. Wolverton, J.P. Greeley, First principles simulations of the electrochemical lithiation and delithiation of faceted crystalline silicon, J. Am. Chem. Soc. 134 (35) (2012) 14362–14374, https://doi.org/10.1021/ja301766z.

[42] V.A. Sethuraman, V. Srinivasan, J. Newman, Analysis of electrochemical lithiation and delithiation kinetics in silicon, J. Electrochem. Soc. 160 (2) (2013) A394, https://doi.org/10.1149/2.008303jes.

[43] A.W. Golubkov, S. Scheikl, R. Planteu, G. Voitic, H. Wiltsche, C. Stangl, G. Fauler, A. Thaler, V. Hacker, Thermal runaway of commercial 18650 Li-ion batteries with LFP and NCA cathodes – impact of state of charge and overcharge, RSC Adv. 5 (70) (2015) 57171–57186, https://doi.org/10.1039/C5RA05897J.

[44] M.E. Wojtala, A.A. Zülke, R. Burrell, M. Nagarathinam, G. Li, H.E. Hoster, D. A. Howey, M.P. Mercer, Entropy profiling for the diagnosis of NCA/Gr-SiO_x Li-ion battery health, J. Electrochem. Soc. 169 (10) (2022) 100527, https://doi.org/10.1149/1945-7111/ac87d1.

[45] B.Y. Kang, H. Jeong, Y. Choi, Y. Ok, J.H. Sung, V.K.A. Muniraj, S.C. Reddy, S. K. Mohanty, M.K. Srinivasa, H.D. Yoo, Entropymetry of active materials for Li-ion batteries, J. Phys. Chem. C (2024), https://doi.org/10.1021/acs.jpcc.3c07682.

[46] L.M. Housel, W. Li, C.D. Quilty, M.N. Vila, L. Wang, C.R. Tang, D.C. Bock, Q. Wu, X. Tong, A.R. Head, et al., Insights into reactivity of silicon negative electrodes: analysis using isothermal microcalorimetry, ACS Appl. Mater. Interfaces 11 (41) (2019) 37567–37577, https://doi.org/10.1021/acsami.9b10772.

[47] M.N. Vila, E.M. Bernardez, W. Li, C.A. Stackhouse, C.J. Kern, A.R. Head, X. Tong, S. Yan, L. Wang, D.C. Bock, et al., Interfacial reactivity of silicon electrodes: impact of electrolyte solvent and presence of conductive carbon, ACS Appl. Mater. Interfaces 14 (18) (2022) 20404–20417, https://doi.org/10.1021/acsami.1c22044.

[48] G. Nuroldayeva, D. Adair, Z. Bakenov, B. Uzakbaiuly, Revealing phase transition in Ni-rich cathodes via a nondestructive entropymetry method, ACS Omega 8 (41) (2023) 37899–37907, https://doi.org/10.1021/acsomega.3c03245.

[49] K. Chen, G. Unsworth, X. Li, Measurements of heat generation in prismatic Li-ion batteries, J. Power Sources 261 (2014) 28–37, https://doi.org/10.1016/j.jpowsour.2014.03.037.

[50] W. Li, L.M. Housel, G.P. Wheeler, D.C. Bock, K.J. Takeuchi, E.S. Takeuchi, A. C. Marschilok, Thermodynamic analysis of $LiNi_{0.6}Mn_{0.2}Co_{0.2}O_2$ (NMC622) voltage hysteresis induced through high voltage charge, ACS Appl. Energy Mater. 4 (11) (2021) 12067–12073, https://doi.org/10.1021/acsaem.1c02334.
[51] D.J. Arnot, E.S. Takeuchi, A.C. Marschilok, K.J. Takeuchi, Isothermal microcalorimetric analysis of Li/CF_x battery discharge, J. Electrochem. Soc. 170 (6) (2023) 060505, https://doi.org/10.1149/1945-7111/acd813.
[52] C. Love, D. Hayman, Battery Test Manual for Baselining and Benchmarking Pre-commercial Cells, 2022. NRL/6170/MR-2022/8.
[53] USABC Electric Vehicle Battery Test Procedures; INL/EXT-15-34184 (2020).
[54] J. Christophersen, Battery Test Manual For Electric Vehicles; INL/EXT-15-34184 (2015).
[55] O. Munteshari, J. Lau, A. Krishnan, B. Dunn, L. Pilon, Isothermal calorimeter for measurements of time-dependent heat generation rate in individual supercapacitor electrodes, J. Power Sources 374 (2018) 257–268, https://doi.org/10.1016/j.jpowsour.2017.11.012.
[56] S.W. Baek, K.E. Wyckoff, D.M. Butts, J. Bienz, A. Likitchatchawankun, M. B. Preefer, M. Frajnkovič, B.S. Dunn, R. Seshadri, L. Pilon, Operando calorimetry informs the origin of rapid rate performance in microwave-prepared $TiNb_2O_7$ electrodes, J. Power Sources 490 (2021) 229537, https://doi.org/10.1016/j.jpowsour.2021.229537.
[57] R. Carter, E.J. Klein, T.A. Kingston, C.T. Love, Detection of lithium plating during thermally transient charging of Li-ion batteries, Front. Energy Res. 7 (2019), https://doi.org/10.3389/fenrg.2019.00144.
[58] Y. Reynier, J. Graetz, T. Swan-Wood, P. Rez, R. Yazami, B. Fultz, Entropy of Li intercalation in Li_xCoO_2, Phys. Rev. B 70 (17) (2004) 174304, https://doi.org/10.1103/PhysRevB.70.174304.
[59] P. Shafiei Sabet, G. Stahl, D.U. Sauer, Non-invasive investigation of predominant processes in the impedance spectra of high energy lithium-ion batteries with nickel–cobalt–aluminum cathodes, J. Power Sources 472 (2020) 228189, https://doi.org/10.1016/j.jpowsour.2020.228189.
[60] A. Grenier, H. Liu, K.M. Wiaderek, Z.W. Lebens-Higgins, O.J. Borkiewicz, L.F. J. Piper, P.J. Chupas, K.W. Chapman, Reaction heterogeneity in $LiNi_{0.8}Co_{0.15}Al_{0.05}O_2$ induced by surface layer, Chem. Mater. 29 (17) (2017) 7345–7352, https://doi.org/10.1021/acs.chemmater.7b02236.
[61] K.P.C. Yao, J.S. Okasinski, K. Kalaga, J.D. Almer, D.P. Abraham, Operando quantification of (De)Lithiation behavior of silicon–graphite blended electrodes for lithium-ion batteries, Adv. Energy Mater. 9 (8) (2019) 1803380, https://doi.org/10.1002/aenm.201803380.
[62] D. Uxa, B. Jerliu, E. Hüger, L. Dörrer, M. Horisberger, J. Stahn, H. Schmidt, On the lithiation mechanism of amorphous silicon electrodes in Li-ion batteries, J. Phys. Chem. C 123 (36) (2019) 22027–22039, https://doi.org/10.1021/acs.jpcc.9b06011.
[63] C. Gan, C. Zhang, W. Wen, Y. Liu, J. Chen, Q. Xie, X. Luo, Enhancing delithiation reversibility of $Li_{15}Si_4$ alloy of silicon nanoparticles-carbon/graphite anode materials for stable-cycling lithium ion batteries by restricting the silicon particle size, ACS Appl. Mater. Interfaces 11 (39) (2019) 35809–35819, https://doi.org/10.1021/acsami.9b13750.
[64] J. Moon, H.C. Lee, H. Jung, S. Wakita, S. Cho, J. Yoon, J. Lee, A. Ueda, B. Choi, S. Lee, et al., Interplay between electrochemical reactions and mechanical responses in silicon–graphite anodes and its impact on degradation, Nat. Commun. 12 (1) (2021) 2714, https://doi.org/10.1038/s41467-021-22662-7.
[65] V. Müller, R.-G. Scurtu, K. Richter, T. Waldmann, M. Memm, M.A. Danzer, M. Wohlfahrt-Mehrens, Effects of mechanical compression on the aging and the expansion behavior of Si/C-Composite|NMC811 in different lithium-ion battery cell formats, J. Electrochem. Soc. 166 (15) (2019) A3796, https://doi.org/10.1149/2.1121915jes.
[66] L. Willenberg, P. Dechent, G. Fuchs, M. Teuber, M. Eckert, M. Graff, N. Kürten, D. U. Sauer, E. Figgemeier, The development of jelly roll deformation in 18650 lithium-ion batteries at low state of charge, J. Electrochem. Soc. 167 (12) (2020) 120502, https://doi.org/10.1149/1945-7111/aba96d.
[67] R. Carter, E.J. Klein, R.W. Atkinson, C.T. Love, Mechanical collapse as primary degradation mode in mandrel-free 18650 Li-ion cells operated at 0 °C, J. Power Sources 437 (2019) 226820, https://doi.org/10.1016/j.jpowsour.2019.226820.
[68] A. Grenier, P.J. Reeves, H. Liu, I.D. Seymour, K. Märker, K.M. Wiaderek, P. J. Chupas, C.P. Grey, K.W. Chapman, Intrinsic kinetic limitations in substituted lithium-layered transition-metal oxide electrodes, J. Am. Chem. Soc. 142 (15) (2020) 7001–7011, https://doi.org/10.1021/jacs.9b13551.
[69] R. Amin, D.B. Ravnsbæk, Y.-M. Chiang, Characterization of electronic and ionic transport in $Li_{1-x}Ni_{0.8}Co_{0.15}Al_{0.05}O_2$ (NCA), J. Electrochem. Soc. 162 (7) (2015) A1163, https://doi.org/10.1149/2.0171507jes.
[70] J.H. Park, H. Yoon, Y. Cho, C.Y. Yoo, Investigation of lithium ion diffusion of graphite anode by the galvanostatic intermittent titration technique, Materials 14 (16) (2021).
[71] C.L. Berhaut, M. Mirolo, D.Z. Dominguez, I. Martens, S. Pouget, N. Herlin-Boime, M. Chandesris, S. Tardif, J. Drnec, S. Lyonnard, Charge dynamics induced by lithiation heterogeneity in silicon-graphite composite anodes, Adv. Energy Mater. 13 (44) (2023) 2301874, https://doi.org/10.1002/aenm.202301874.